

Accepted Article

Title: Programmable Modular Assembly of Homochiral Ir(III)-Metallohelices to Reverse Metallodrug Resistance by Inhibiting CDK1

Authors: Xuezhao Li, Xing Zhao, Xingyun Wang, Anxian Xiong, Zhicheng Wang, Zhuolin Shi, Jingyi Zhang, Hanlin Wang, Wei Wei, Cheng He, Jiajia Ma, Zijian Guo, Chunying Duan, Jing Zhao, and Xiuxiu Wang

This manuscript has been accepted after peer review and appears as an Accepted Article online prior to editing, proofing, and formal publication of the final Version of Record (VoR). The VoR will be published online in Early View as soon as possible and may be different to this Accepted Article as a result of editing. Readers should obtain the VoR from the journal website shown below when it is published to ensure accuracy of information. The authors are responsible for the content of this Accepted Article.

To be cited as: *Angew. Chem. Int. Ed.* **2024**, e202419292

Link to VoR: <https://doi.org/10.1002/anie.202419292>

RESEARCH ARTICLE

Programmable Modular Assembly of Homochiral Ir(III)-Metallohelices to Reverse Metallodrug Resistance by Inhibiting CDK1

Xuezhaoli Li,^{*[a] #} Xing Zhao,^{[a] #} Xingyun Wang,^{[c] #} Anxian Xiong,^[a] Zhicheng Wang,^[c] Zhuolin Shi,^[a] Jingyi Zhang,^[b] Hanlin Wang,^[a] Wei Wei,^[c] Cheng He,^[a] Jiajia Ma,^[d] Zijian Guo,^b Chunying Duan,^{*[a]} Jing Zhao,^{*[b]} Xiuxiu Wang^{*[b]}

- [a] X. Li, X. Zhao, A. Xiong, Z. Shi, H. Wang, C. He, C. Duan
Cancer Hospital of Dalian University of Technology, School of Chemistry, State Key Laboratory of Fine Chemicals, Dalian University of Technology, Dalian 116024, China;
E-mail: xuezhaoli@dlut.edu.cn; cyduan@dlut.edu.cn
- [b] J. Zhang, X. Wang, J. Zhao
Chemistry and Biomedicine Innovation Center (ChemBIC), State Key Laboratory of Coordination Chemistry, School of Chemistry and Chemical Engineering, Nanjing University, Nanjing, 210023, China
Institution
E-mail: wangxiuxiu@nju.edu.cn; jingzhao@nju.edu.cn
- [c] X. Wang, Z. Wang, W. Wei
State Key Laboratory of Pharmaceutical Biotechnology, School of Life Sciences, Nanjing University, Nanjing, 210023, China
- [d] J. Ma
Frontiers Science Center for Transformative Molecules, Shanghai Key Laboratory for Molecular Engineering of Chiral Drugs, School of Chemistry and Chemical Engineering and Zhangjiang Institute for Advanced Study, Shanghai Jiao Tong University, Shanghai 200240, China

These authors contributed equally.

Abstract: Drug resistance is a major cause of cancer recurrence and poor prognosis. The innovative design and synthesis of inhibitors to target drug-resistance-specific proteins is highly desirable. However, challenges remain in precisely adjusting their conformation and stereochemistry to adapt the chiral regions of target proteins. Herein, using a stepwise programmable modular assembly approach, we precisely engineered two pairs of homochiral dinuclear Ir(III) metallohelices ($\Delta_2\text{S}_4\text{-H}_{\text{bpy}}$ and $\Delta_2\text{R}_4\text{-H}_{\text{bpy}}$, $\Delta_2\text{S}_4\text{-H}_{\text{bpy}}$ and $\Delta_2\text{R}_4\text{-H}_{\text{bpy}}$) functionalized with flexible dithiourea linkages. The resulting homochiral metallohelices exhibited significant chirality-dependent photocytotoxicities, and the enhanced structural compatibility of $\Delta_2\text{S}_4\text{-H}_{\text{bpy}}$ with the target cyclin-dependent kinase 1 (CDK1) contributed to its superior photodynamic therapy efficacy, achieving an outstanding photocytotoxicity index (PI) value of 2.3×10^4 . Interestingly, emerging as a critical mediator in the development of oxaliplatin resistance, CDK1 targeting by $\Delta_2\text{S}_4\text{-H}_{\text{bpy}}$ achieved enhanced cellular uptake, anticancer activity, and oncosis-mediated cell death in oxaliplatin-resistant HCT8/L cells. Mechanistic investigations, including proteomic profiling and CDK1 gene silencing, confirmed the pivotal role of chirality-selective CDK1 targeting in reversing metallodrug resistance. This study introduces a promising platform for constructing and customizing flexible metallohelices with precise conformation and stereochemistry to target drug-resistance-specific proteins, offering innovative insights into the designability of metallodrugs to overcome drug resistance.

Introduction

Platinum-based metallodrugs are among the most effective and widely used clinical agents for the treatment of cancer by covalently binding to DNA.^[1] However, their clinical success has been significantly limited by the persistent issue of acquired drug

resistance.^[2] To address this challenge, there is an urgent need for alternative metallodrug designs that differ from platinum compounds and exhibit novel molecular-level interactions.^[3] Photodynamic therapy (PDT) has emerged as a promising cancer treatment strategy, primarily relying on in situ-generated reactive oxygen species (ROS) to irreversibly damage tumors when photosensitizers are activated by light of a specific wavelength.^[4] Emerging evidence has suggested that PDT's unique mechanisms for damaging tumor cells and their microenvironments could help overcome cancer drug resistance, mitigate compensatory survival pathways, and even resensitize resistant cells to standard therapies.^[5] For instance, PDT can directly damage antiapoptotic B-cell lymphoma-2 (BCL-2) proteins and the drug efflux pumps involved in classical drug resistance.^[5-6] Recent studies have also identified the inhibition of cyclin-dependent kinase 1 (CDK1) as a potential strategy to treat patients with oxaliplatin-resistant colorectal cancer (CRC).^[7] In this context, the innovative design and synthesis of newly formed metallodrugs capable of efficiently inhibiting or directly photodamaging drug-resistance-specific proteins is highly desirable. Benefiting from their significantly enhanced three-dimensional (3D) geometries compared to purely organic molecules, kinetically inert octahedral mononuclear complexes of Ir(III), Ru(II), and Rh(III) with tailored structures and stereochemistry have demonstrated impressive abilities in selectively inhibiting protein kinases, such as tumor necrosis factor- α (TNF- α), by effectively occupying protein pockets.^[8] In the pursuit of selectively and potently modulating resistance-specific

RESEARCH ARTICLE

protein functions with exclusive targeting precision, challenges still remain in designing metallodrug compounds with precise conformations and stereochemistry to fit target protein 3D regions.^[9] Further precision engineering and rational tailoring of inhibitory molecules with more complex conformations and stereoconfiguration are pivotal to fully exploit their potential in targeting intricate chiral protein pockets.^[10]

Supramolecular chemistry, in contrast to traditional covalent synthesis, offers advanced design possibilities for creating multinuclear supramolecular assemblies with elaborate sizes and shapes that can closely mimic biomolecular recognition motifs, resulting in enhanced binding sensitivity and stereoselectivity towards biomolecules.^[11] Notably, metallohelices, which are promising nonpeptide α -helix mimetics, possess intrinsic chirality and offer tunable 3D configurations, diameters, charges, and amphipathicity.^[12] Particularly, their helical conformations may lead to enhanced binding affinity and selectivity for biomolecule targets while preserving sufficient bioavailability to reach intracellular locations.^[13] Metallohelices have unveiled remarkable non-covalent targeting capabilities towards DNA and proteins, resulting in striking enantiomer-dependent anticancer or antibiotic activities.^[14] To fully unlock their unique bioactivities, it is crucial to precisely control and tailor their stereochemistry during synthesis and maintain this chirality throughout treatment cycles.^[15] Additionally, ideal metallohelices should exhibit sufficient conformational complexity and flexibility, as well as multiple binding sites, enabling stronger structural compatibility and interactions with protein residues.^[16]

Herein, as depicted in Figure 1, we designed and controllably synthesized two pairs of homochiral, double-stranded, dinuclear Ir(III)-metallohelices, exhibiting sufficient structure flexibility and refined stereoconfigurations. These flexible Ir(III) metallohelices were constructed using a stepwise programmable modular assembly (PMA) approach by alternately varying the preprogrammed enantiopure Ir(III) modules (Λ - or Δ -configuration) with chiral *trans*-1,2-cyclohexanediamine (DACH, *RR/SS*-forms) connectors. Importantly, these structurally well-engineered metallohelices displayed significant chirality-dependent photocytotoxicity toward A549 cancer cells and, notably, potent efficacy against oxaliplatin-resistant HCT8/L cells. Mechanistic studies suggested that the specific chiral conformation of homochiral metallohelices, particularly $\Delta_2\text{S}_4\text{-H}_{\text{bpy}}$, led to enhanced structural compatibility with CDK1, contributing to their distinct anticancer activity. As a critical mediator in the development of oxaliplatin resistance, CDK1's high-affinity for $\Delta_2\text{S}_4\text{-H}_{\text{bpy}}$ contributed to the enhanced cellular uptake and anticancer activity against oxaliplatin-resistant HCT8/L cells.

Further mechanistic investigations, including proteomic profiling and CDK1 gene silencing, confirmed the pivotal role of chirality-selective CDK1 targeting in reversing metallodrug resistance. This flexible synthetic strategy provides a unique approach to aligning the conformations and chirality of metallohelices with specific protein regions, thereby offering innovative insights into the designability of targeting specific proteins and potent anticancer PDT effects. Impressively, by selectively binding to CDK1, a strong ability to reverse anticancer drug resistance can be achieved.

Results and Discussion

Design and Synthesis of Flexible Ir(III)-metallohelices.

Generally, homochiral metallohelices are formed by mechanically coupling relatively rigid, short chiral ligands with kinetically labile metal ions.^[17] In one hand, the inherent dynamic activity of the coordination bonds allows for self-correction during the assembly process, leading to thermodynamically controlled architectures. However, the dynamic nature of coordination bonds makes them susceptible to external factors such as light, concentration, acidity or basicity, which can cause the decomposition of the helicate molecules.^[18] On the other hand, while rigid and short ligands are effective at facilitating the chiral transfer from ligands to metal vertices, the resulting metallohelices tend to have rigid skeletons.^[14f, 19] In order to maximize the binding affinity between the metallohelices and targeted proteins, robust but structurally flexible metallohelices are highly desirable.^[14b, 16] In continuance of our efforts to develop photoactive and homochiral Ir(III)-based metallohelices,^[14e, 14f, 20] we introduced two thiourea groups as the linkages to connect enantiopure Ir(III) modules and DACH spacers by using an programmable modular assembly approach. We envisioned that by alternately varying the preprogrammed enantiopure Ir(III) modules (Λ/Δ -configuration) with chiral DACH connectors (*RR/SS*-forms), four homochiral metallohelices, $\Delta_2\text{S}_4\text{-H}_{\text{bpy}}/\Lambda_2\text{R}_4\text{-H}_{\text{bpy}}$ and $\Lambda_2\text{S}_4\text{-H}_{\text{bpy}}/\Delta_2\text{R}_4\text{-H}_{\text{bpy}}$, could be obtained controllably. Importantly, the enantiomerically pure DACH spacers position two thiourea groups configurationally located on the opposite sides of the cyclohexane plane, thus functionalizing the helicans with abundant potential H-bond donors and acceptors, which are expected to enhance binding affinity toward residues in the protein active pocket.^[16c]

Enantiomerically pure $[\text{Ir}(\text{ppy})_2(\text{bpy})][\text{PF}_6]$ reference complexes (Λ -Ir and Δ -Ir, where ppy = phenylpyridine, bpy = 2,2'-bipyridine) and the NCS groups (NCS = isothiocyanate) end-capped mononuclear Ir(III) modules $[\text{Ir}(\text{ppy}-\text{NCS})_2(\text{bpy})][\text{PF}_6]$ (Λ -Ir-NCS and Δ -Ir-NCS) were synthesized according to the method

RESEARCH ARTICLE

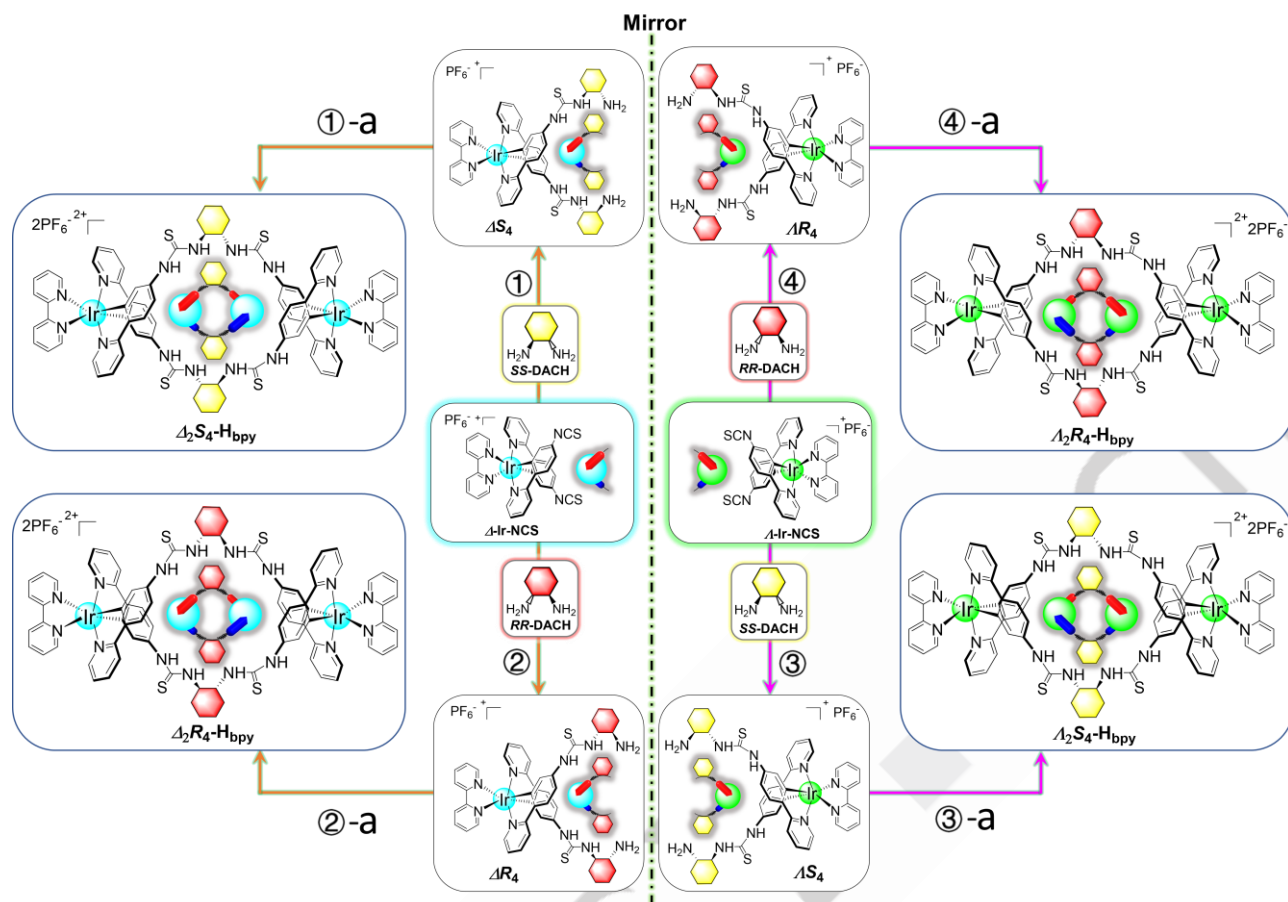


Figure 1. Programmable modular assembly of homochiral, flexible dinuclear Ir(III)-metallohelices. Enantiopure Λ - or Δ -Ir-NCS modules are connected with RR-DACH or SS-DACH spacers to yield two pairs of enantiopure mononuclear Ir(III)-hemihelices: $\Delta S_4/\Lambda R_4$ and $\Lambda S_4/\Delta R_4$ at the first stage. These secondary building units are then used in further reactions with alternating Δ - or Λ -Ir-NCS modules, resulting in the two pairs of homochiral dinuclear Ir(III)-metallohelices: $\Delta_2 S_4\text{-H}_{bpy}/\Lambda_2 R_4\text{-H}_{bpy}$ and $\Lambda_2 S_4\text{-H}_{bpy}/\Delta_2 R_4\text{-H}_{bpy}$. Cartoon representations show RR-DACH and SS-DACH in red and yellow respectively, with Ir atoms colored green (Λ -handed) and cyan (Δ -handed).

reported by Meggers and coworkers (Supplementary Section 2.1 and 2.2).^[21] Subsequently, as shown in Figure 1 along synthetic paths 1 to 4, a series of reactions involving the free combination of Λ -Ir-NCS and Δ -Ir-NCS with RR- or SS-DACH alternately in CH_2Cl_2 were conducted, leading to the smooth formation of two pairs of enantiopure mononuclear Ir(III) hemihelices: $\Delta S_4/\Lambda R_4$ and $\Lambda S_4/\Delta R_4$. Using these secondary building units and a procedural approach involving further reactions with Δ - or Λ -Ir-NCS, we selectively obtained two pairs of homochiral dinuclear Ir(III)-metallohelices: $\Delta_2 S_4\text{-H}_{bpy}/\Lambda_2 R_4\text{-H}_{bpy}$ and $\Lambda_2 S_4\text{-H}_{bpy}/\Delta_2 R_4\text{-H}_{bpy}$. For example, the reaction of ΔS_4 and Δ -Ir-NCS in a 1:1 ratio in CH_2Cl_2 at room temperature provided $\Delta_2 S_4\text{-H}_{bpy}$ in a yield of 59% (path 1-a). Similarly, the reaction of ΛR_4 and Λ -Ir-NCS produced the enantiomer $\Lambda_2 R_4\text{-H}_{bpy}$ with a yield of 54% (path 4-a). Homochiral $\Delta_2 R_4\text{-H}_{bpy}$ and $\Lambda_2 S_4\text{-H}_{bpy}$ were also controllably obtained via similar approaches, as shown in paths 2-a and 3-a, respectively. The enantiopure mononuclear Ir(III) species and the homochiral dinuclear Ir(III) metallohelices were thoroughly characterized using high-resolution electrospray ionization mass spectrometry

(HR-ESI-MS), nuclear magnetic resonance (NMR) and high-performance liquid chromatography (HPLC), as detailed in the Supplementary Information, confirming their formation and purity.

X-ray Crystal Structures of Metallohelices.

Attempts to obtain crystals of the homochiral metallohelices described above were unsuccessful. However, to gain insight into their 3D structures, cocrystallization of $\Lambda_2 S_4\text{-H}_{bpy}$ and $\Delta_2 R_4\text{-H}_{bpy}$, as well as $\Delta_2 S_4\text{-H}_{bpy}$ and $\Lambda_2 R_4\text{-H}_{bpy}$, by vapor diffusion of diethyl ether into DMF-DMSO solutions of the respective complexes, successfully yielded crystals suitable for X-ray diffraction analysis. As shown in Figure 2a, two SS-DACH spacers are equipped within the helicands of $\Lambda_2 S_4\text{-H}_{bpy}$ and coupled with two Ir(III) modules with the same Λ -configurations. Similarly, the RR-DACH spacers link two Δ -Ir-NCS units to form the homochiral $\Delta_2 R_4\text{-H}_{bpy}$. Notably, the SS-DACH-functionalized dithiurea helicands of $\Lambda_2 S_4\text{-H}_{bpy}$ adopt a smooth "V"-type arrangement, which separates the two Ir(III) atoms by a distance of 12.74 Å, and with a dihedral angle approximately 75.46° between the two bpy planes.

RESEARCH ARTICLE

Interestingly, the SS-DACH-decorated helicands adopt an “L”-shaped arrangement, result in a narrower distance of 10.98 Å between the two Ir(III) atoms in $\Delta_2\text{S}_4\text{-H}_{\text{bpy}}$, with a dihedral angle between the two bpy-planes at approximately 77.16° (Figure 2b). A closer examination reveals key structural differences, as shown in Figure S97 and Figure S98. In both $\Lambda_2\text{S}_4\text{-H}_{\text{bpy}}$ and $\Delta_2\text{S}_4\text{-H}_{\text{bpy}}$, the SS-DACH spacers position two thiourea groups on opposite sides of the cyclohexane plane. However, the orientation of the 'H' atoms relative to the 'S' atoms in the thiourea groups differs significantly. In $\Lambda_2\text{S}_4\text{-H}_{\text{bpy}}$, all 'H' atoms adopt a “syn” conformation

relative to the 'S' atoms, whereas in $\Delta_2\text{S}_4\text{-H}_{\text{bpy}}$, two 'H' atoms adopt a “syn” conformation and the other two adopt an “anti” conformation within the helicands. By using flexible dithiourea group as linkages to connect enantiopure Ir(III) modules with chiral DACH connectors, two pairs homochiral metallohelicels with significantly different conformations can be successfully constructed. Furthermore, the helicands, featuring a chiral cyclohexane skeleton functionalized with numerous potential H-bond donors and acceptors, are expected to enhance binding affinity toward residues in the protein active pocket.^[16c]

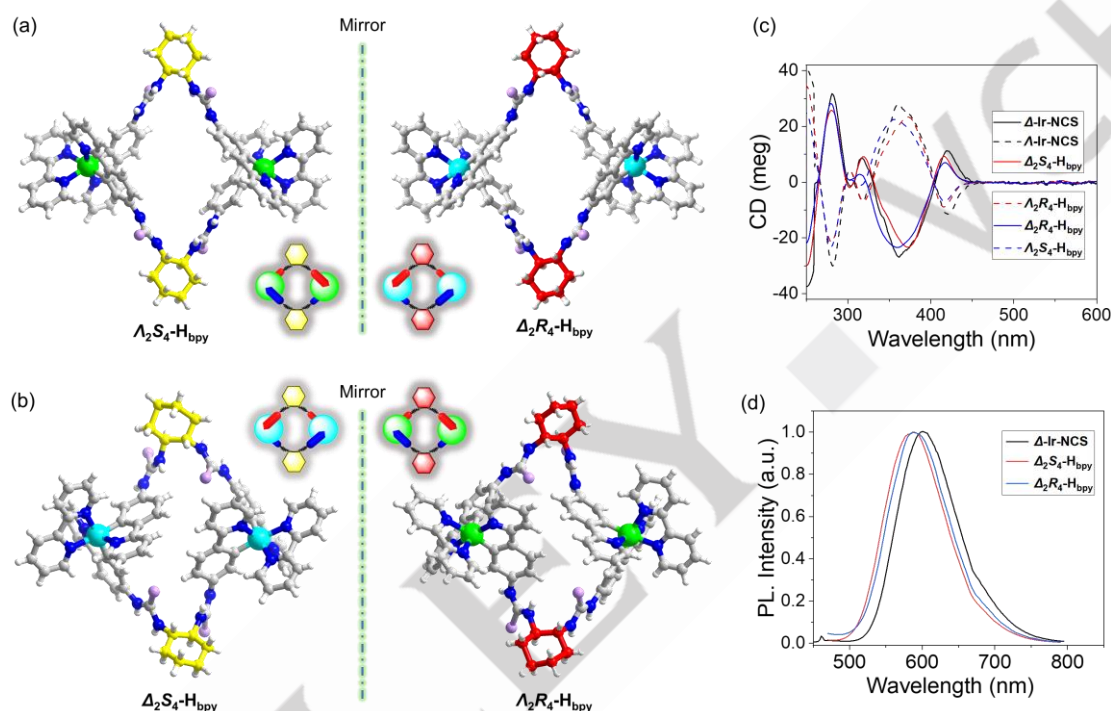


Figure 2. Single-crystal x-ray structures, CD and luminescent spectral characterizations. (a, b) The crystal structures and their cartoon representations of homochiral metallohelicels. Atom colors: C = gray, H = white, N = blue, S = purple, Ir = green (Λ -handed) and cyan (Δ -handed). Solvent and counteranion molecules are omitted for clarity. *RR*-DACH and *SS*-DACH are drawn in red and yellow, respectively. (c) CD spectra of the starting enantiomeric mononuclear modules and homochiral metallohelicels in DMSO. (d) Normalized photoluminescence spectra of representative Ir(III) complexes in DMSO.

CD and spectral characterization.

In DMSO solution, both $\Lambda_2\text{R}_4\text{-H}_{\text{bpy}}/\Delta_2\text{S}_4\text{-H}_{\text{bpy}}$ and $\Lambda_2\text{S}_4\text{-H}_{\text{bpy}}/\Delta_2\text{R}_4\text{-H}_{\text{bpy}}$ exhibited mirror-image CD spectra with robust Cotton effects, closely resembling those of the initial mononuclear Λ -/ Δ -Ir-NCS modules. As shown in Figure 2c, Δ -Ir-NCS displayed three positive Cotton effects at 281, 317 and 420 nm, along with an intense negative CD band at 362 nm. In comparison, $\Delta_2\text{S}_4\text{-H}_{\text{bpy}}$ exhibited three primary positive Cotton effects at 280, 318, and 416 nm, followed by two negative bands at 303 and 373 nm. The first three bands correspond to the $n\text{-}\pi^*$ and $\pi\text{-}\pi^*$ transitions of the ppy and bpy groups, while the Cotton effect at longer wavelengths originates from the metal-to-ligand charge transfer (MLCT) bands. Notably, the resulting metallohelicels $\Delta_2\text{R}_4\text{-H}_{\text{bpy}}$ and $\Lambda_2\text{S}_4\text{-H}_{\text{bpy}}$ exhibited similar CD bands at 279, 359, and 417

nm when compared to those of $\Delta_2\text{S}_4\text{-H}_{\text{bpy}}$ and $\Lambda_2\text{R}_4\text{-H}_{\text{bpy}}$, respectively. The highly symmetrical and similar CD curves suggest that the pseudo-octahedral iridium stereochemistry of the starting Λ -/ Δ -Ir-NCS modules was well preserved during the assembly process, dominating the chirality of these enantiopure metallohelicels.^[11d]

Unlike previously reported metallohelicels with first-row metal ions as vertices,^[12, 22] the introduction of photoactive [Ir(ppy)₂(bpy)]PF₆ imparts promising luminescent emission properties to these metallohelicels. Taking the mononuclear Δ -Ir-NCS module and the helical $\Delta_2\text{S}_4\text{-H}_{\text{bpy}}$, $\Delta_2\text{R}_4\text{-H}_{\text{bpy}}$ as examples, the luminescence spectra of Δ -Ir-NCS exhibited a broad, featureless emission centered at $\lambda = 603$ nm when excited at $\lambda = 405$ nm under anaerobic conditions. Similarly, the luminescence

RESEARCH ARTICLE

spectra of $\Delta_2S_4\text{-H}_{\text{bpy}}$ and $\Delta_2R_4\text{-H}_{\text{bpy}}$ presented similar broad peaks at $\lambda = 587$ and 590 nm, respectively (Figure 2d, Supplementary Section 4.2). Importantly, these luminescent metallohelices demonstrated high photo- and chemical stability (Supplementary

Section 5). Moreover, given their diverse conformations and stereochemistries, these homochiral metallohelices may provide promising opportunities for investigation of the structure–function relationship with proteins as therapeutic agents.

Table 1. IC_{50} values of the homochiral metallohelices and the enantiopure mononuclear Ir(III) complexes toward A549 cells with light irradiation (white light, 30 mW/cm^2 , 30 min) and in the dark.

IC_{50}	$\Lambda_2S_4\text{-H}_{\text{bpy}}$	$\Lambda_2R_4\text{-H}_{\text{bpy}}$	$\Delta_2S_4\text{-H}_{\text{bpy}}$	$\Delta_2R_4\text{-H}_{\text{bpy}}$	$\Delta\text{-Ir}$	$\Lambda\text{-Ir}$
Light (nM)	96.0 ± 5.1	178.0 ± 8.4	8.7 ± 1.2	367.0 ± 9.1	164.0 ± 5.8	19.0 ± 2.6
Dark (μM)	>200	>200	>200	>200	1.2 ± 0.2	1.5 ± 0.1
PI	>2080	>1120	>23000	>545	>7	>79

In vitro and in vivo Anticancer Activities

The $(IC_{50})_{\text{dark}}$ values of these homochiral metallohelices in A549 cells all displayed negligible toxicity (>200 μM) compared to the corresponding mononuclear Ir(III) complexes, $\Delta\text{-Ir}$ and $\Lambda\text{-Ir}$, which exhibited $(IC_{50})_{\text{dark}}$ values of 1.2 μM and 1.5 μM , respectively. However, the metallohelices demonstrated significantly chirality induced photocytotoxicity. It is worth noting that the extraordinary $(IC_{50})_{\text{irrad}}$ value of $\Delta_2S_4\text{-H}_{\text{bpy}}$ was only 8.7 nM, resulting in a

photocytotoxicity index (PI, ratio of $(IC_{50})_{\text{dark}}/(IC_{50})_{\text{irrad}}$) exceeding 23000 (Table 1, and Figure 3a). Given the luminescence of metallohelices, we also detected the subcellular localization of complexes in cells. As displayed in Figure S123, the metallohelices are mainly located in the cytoplasm and the uptake of $\Delta_2S_4\text{-H}_{\text{bpy}}$ conformation was higher than the other three metallohelices. These results underscore the high chiral selectivity of metallohelices in photodriven cytotoxicity.

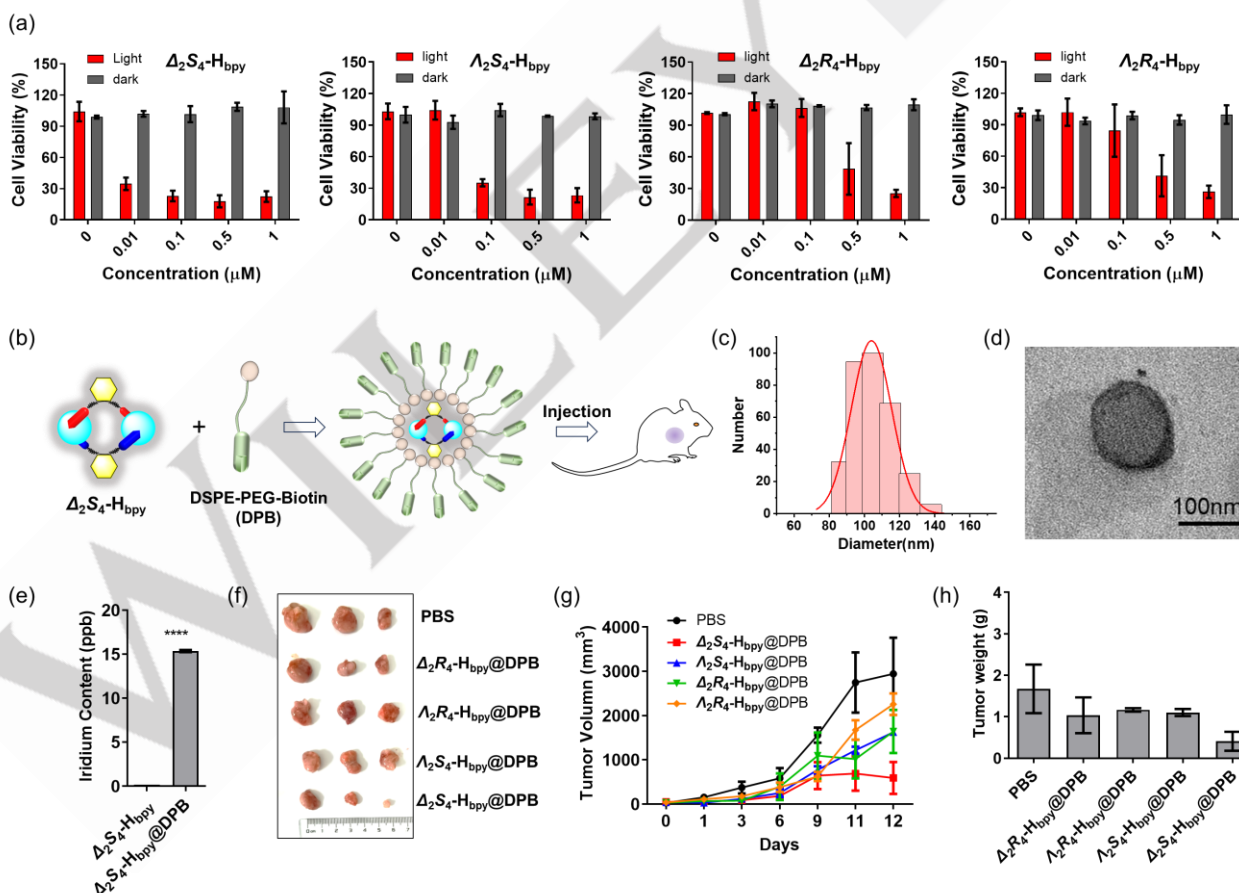


Figure 3. Chirality-dependent anticancer activity of metallohelices *in vitro* and *in vivo*. (a) Cell viability of metallohelices toward A549 cells after treatment with various concentrations. (b) Schematic illustration of the encapsulating process for metallohelices. (c) Dynamic light scattering characterization of encapsulated $\Delta_2S_4\text{-H}_{\text{bpy}}$. (d) TEM characterization of encapsulated $\Delta_2S_4\text{-H}_{\text{bpy}}$. (e) Accumulation of $\Delta_2S_4\text{-H}_{\text{bpy}}$ in tumor sites with or without encapsulation. (f) Representative tumor images after 12 d of treatment in A549 tumor-bearing mice. (g) Time-dependent growth of tumor volume in mice with treatments. (h) Weights of tumor tissues after 12 days of treatment. Data are mean \pm s.d. ($n = 3$). * $P < 0.05$, ** $P < 0.01$, *** $P < 0.001$, analyzed by Student's test. Light source: White light, 30 mW/cm^2 , 30 min.

RESEARCH ARTICLE

To further investigate their potential as PDT agents, the ability of the four homochiral metallohelices in inducing ROS was assessed. As shown in Figure S124, $\Delta_2\text{S}_4\text{-H}_{\text{bpy}}$ induced $87.6 \pm 0.8\%$ production of ROS in cells, with Rosup as the positive control. In contrast, the ROS production induced by $\Lambda_2\text{S}_4\text{-H}_{\text{bpy}}$, $\Delta_2\text{R}_4\text{-H}_{\text{bpy}}$ and $\Lambda_2\text{R}_4\text{-H}_{\text{bpy}}$ was only $43.4 \pm 1.4\%$, $15.3 \pm 4.5\%$, and $2.8 \pm 0.5\%$, respectively. The induction of ROS led to the corresponding cell apoptosis, and the percentage of apoptotic cells also displayed chiral dependence, with the highest percentage of late apoptotic cells observed in $\Delta_2\text{S}_4\text{-H}_{\text{bpy}}$ -treated cells (Figure S125).

Given the impressive *in vitro* photodynamic anticancer activity of these chiral metallohelices, we next explored their chirality-driven therapeutic effects *in vivo*. In this work, to enhance the solubility, bioavailability and tumor targeting of the homochiral metallohelices, we encapsulated metallohelices by using biotin-functionalized polymer DSPE-PEG₂₀₀₀-Biotin (DPB), which is responsible for cancer-specific uptake and facilitates tumor targeting.^[23] After wrapping the metallohelices with DSPE-PEG-biotin, we successfully obtained encapsulated nanoformulations of four metallohelices ($\Delta_2\text{S}_4\text{-H}_{\text{bpy}}\text{@DPB}$, $\Lambda_2\text{R}_4\text{-H}_{\text{bpy}}\text{@DPB}$, $\Delta_2\text{R}_4\text{-H}_{\text{bpy}}\text{@DPB}$, and $\Lambda_2\text{S}_4\text{-H}_{\text{bpy}}\text{@DPB}$) with an average size of approximately 100 nm-200 nm by dynamic light scattering characterization (Figure 3b and 3c). In addition, the morphology and the elemental distribution were also characterized by transmission electron microscope (TEM) and scanning electron microscopy (SEM) analysis, which confirmed the successful wrapping of metallohelices inside (Figure 3d and Figure S126-128). To obtain accurate loading efficiency of metallohelices in DPB, we conducted the quantification of Ir by Inductively coupled plasma-Mass Spectrometry (ICP-MS) analysis, and the calculated loading efficiency of metallohelices was 29.67% for $\Delta_2\text{S}_4\text{-H}_{\text{bpy}}$, 30.87% for $\Lambda_2\text{S}_4\text{-H}_{\text{bpy}}$, 34.99% for $\Delta_2\text{R}_4\text{-H}_{\text{bpy}}$, and 27.27% for $\Lambda_2\text{R}_4\text{-H}_{\text{bpy}}$, respectively (Table S3). The content of metallohelices was then unified to conduct the subsequent analysis. After encapsulation, the uptake of metallohelices in cells was significantly enhanced while the subcellular localization of four metallohelices@DPB was not significantly influenced when compared to metallohelices without wrapping (Figure S129). Impressively, as displayed in Figure 3e, the accumulation of $\Delta_2\text{S}_4\text{-H}_{\text{bpy}}\text{@DPB}$ in tumor tissue was approximately 82-fold higher than that of $\Delta_2\text{S}_4\text{-H}_{\text{bpy}}$ without DSPE-PEG-Biotin encapsulation, underscoring the significant enhancement of tumor targeting by DPB modification. As a result, $\Delta_2\text{S}_4\text{-H}_{\text{bpy}}\text{@DPB}$ exhibited optimal anticancer activity when compared to PBS, $\Lambda_2\text{R}_4\text{-H}_{\text{bpy}}\text{@DPB}$, $\Lambda_2\text{S}_4\text{-H}_{\text{bpy}}\text{@DPB}$ and $\Delta_2\text{R}_4\text{-H}_{\text{bpy}}\text{@DPB}$ from the recording of tumor morphology, volume curves and tumor weights, confirming the chirality-based PDT effect *in vivo* (Figure 3f-h and Figure S130). Altogether, the

superior anticancer effect of $\Delta_2\text{S}_4\text{-H}_{\text{bpy}}$ highlights the critical role of chirality in PDT, offering promising opportunities for the development of chiral-specific photodynamic agents.

Target Proteins of Homochiral $\Delta_2\text{S}_4\text{-H}_{\text{bpy}}$ in the PDT Process Screened by Proteomic Analysis

Considering the chirality-dependent photodynamic effects of the four metallohelices observed *in vitro* and *in vivo*, we next attempted to elucidate the specific molecular mechanism underlying the high activity of $\Delta_2\text{S}_4\text{-H}_{\text{bpy}}$ by employing cellular proteomics analysis methods. By analyzing the differential proteins expressed in $\Delta_2\text{S}_4\text{-H}_{\text{bpy}}$ -treated cells, we screened out 60 upregulated proteins and 120 downregulated proteins (Figure S131-S132 and Table S4). Through bioinformatic analysis of these differentially expressed proteins in Gene Ontology (GO) enrichment, the biological processes in the cell cycle, mitotic cell cycle, cell division, and DNA repair were significantly downregulated (Figure 4a and Table S4). Further pathway analysis using Kyoto Encyclopedia of Genes and Genomes (KEGG) also demonstrated the retardation of the cell cycle, amino acid and pyrimidine metabolism, and DNA replication pathways (Figure 4b). All of these screened pathways point straight at the cell cycle, DNA replication, and cell division, which are fundamental and essential processes in life. We speculate that the crucial proteins and kinases coexisting in these significantly downregulated pathways are the potential targets of $\Delta_2\text{S}_4\text{-H}_{\text{bpy}}$.

To precisely identify the specific targets of $\Delta_2\text{S}_4\text{-H}_{\text{bpy}}$, we further conducted an in-depth analysis of protein-protein interactions (PPIs) among the above differentially expressed proteins. The results highlighted that cell division control protein 45 (CDC45), dual specificity protein kinase (TTK), and cyclin-dependent kinase 1 (CDK1) were the most significantly downregulated proteins (green) (Figure 4c). Additionally, kinetochore protein NDC80 (NDC80) and DNA polymerase epsilon catalytic subunit (POLE) were also notably inhibited in the screened pathways (Tables S3 and S4). The inhibition of these potential targets was then verified by western blot. As indicated in Figure 4d, in contrast to $\Lambda_2\text{R}_4\text{-H}_{\text{bpy}}$ and $\Lambda_2\text{S}_4\text{-H}_{\text{bpy}}$, a pronounced inhibition of CDC45, POLE, TTK, and NDC80 was observed in their enantiomers $\Delta_2\text{S}_4\text{-H}_{\text{bpy}}$ and $\Delta_2\text{R}_4\text{-H}_{\text{bpy}}$.

However, it is noteworthy that, in terms of cyclin-dependent kinase 1 (CDK1) inhibition, only $\Delta_2\text{S}_4\text{-H}_{\text{bpy}}$ demonstrated a significant inhibitory effect and showed a surprisingly chirality-dependent difference (Figure 4d). And this selective inhibition was only presented at the protein level other than DNA/RNA level since the mRNA transcription was not significantly affected by metallohelices (Figure S133). In addition, the crosslink of $\Delta_2\text{S}_4\text{-H}_{\text{bpy}}$

RESEARCH ARTICLE

H_{bpy} with CDK1 also confirmed the interaction of chiral metallohelic with CDK1 protein (Figure S134). These results suggest that the precise regulation and control of the conformation and stereochemistry of metallohelic are responsible for the significant differences in kinase inhibition. Considering the aforementioned differences in PDT activities *in vitro* and *in vivo*, CDK1 might be the key target responsible for the superior PDT activity exhibited by **Δ₂S₄-H_{bpy}**, which inspired us to deeply explore the structural-function interaction of metallohelic with cyclin-dependent kinase.

Molecular Mechanism

First, to reveal the affinity of the four chiral metallohelic with CDK1, we employed Surface Plasmon Resonance (SPR)

biosensor analysis, which provides a highly sensitive and label-free method for the real-time detection of molecular interactions. We initially facilitated the expression and subsequent purification of recombinant human CDK1 protein. The binding affinity of 50 μg/mL of the protein was scrutinized utilizing SPR, and the dissociation constant (K_D) for the **Δ₂S₄-H_{bpy}** complex was determined to be 2.36×10^{-6} M, with an association rate constant (K_a) of 2.11×10^5 M⁻¹ s⁻¹ and a dissociation rate constant (K_d) of 0.499 s⁻¹. These values indicate a markedly stronger binding affinity of **Δ₂S₄-H_{bpy}** for CDK1 relative to the other three chiral metallohelic **Δ₂R₄-H_{bpy}**, **Λ₂R₄-H_{bpy}**, and **Λ₂S₄-H_{bpy}** (Figure 5a-b).

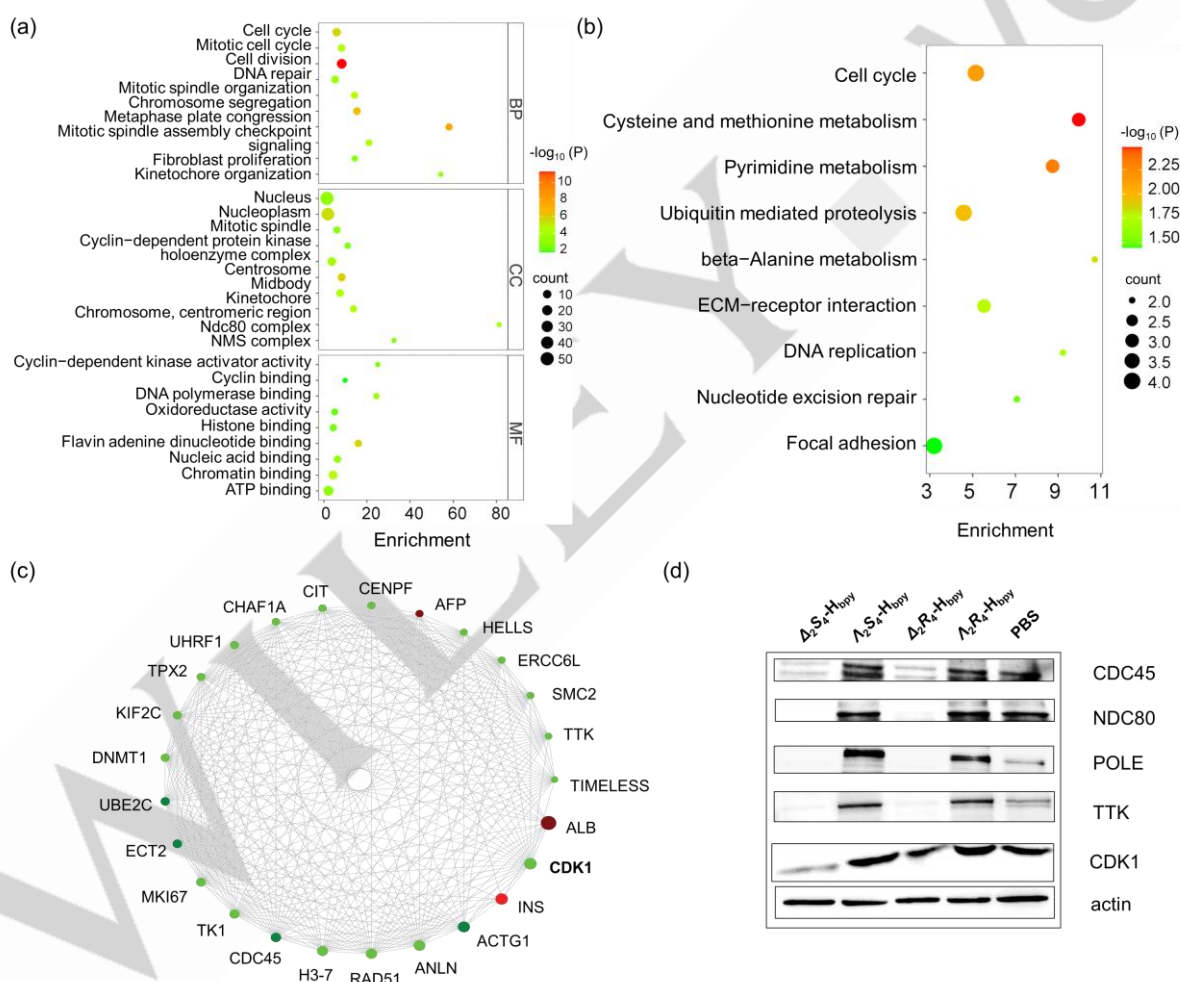


Figure 4. Mechanism excavation of **Δ₂S₄-H_{bpy} in A549 cells by cellular proteomic profiling.** (a) GO enrichment analysis of downregulated proteins in **Δ₂S₄-H_{bpy}**-treated A549 cells. (b) KEGG pathway analysis of differentially expressed proteins in **Δ₂S₄-H_{bpy}**-treated A549 cells. (c) PPI analysis of differentially expressed proteins in **Δ₂S₄-H_{bpy}**-treated A549 cells. (d) Western blot verification of the expression of CDC45, POLE, TTK, NDC80 and CDK1 in A549 cells with treatments.

The detailed binding mode of metallohelic with CDK1 was then investigated by molecular simulations. First, molecular docking demonstrated that **Δ₂S₄-H_{bpy}** is capable of engaging in three hydrogen bond interactions with specific amino acid

residues within the CDK1 protein. The hydrogen atoms located on the benzene ring of **Δ₂S₄-H_{bpy}** establish carbon-hydrogen bonds with GLU8 and SER84 of CDK1, with hydrogen bond lengths of 3.0 and 2.9 Å respectively. Moreover, the thiol group

RESEARCH ARTICLE

present in the $\Delta_2\text{S}_4\text{-H}_{\text{bpy}}$ structure is positioned to form a hydrogen bond with GLU8 of the protein at a distance of 3.8 Å, and the benzene ring engages in a conjugated interaction with LYS9 of CDK1 (Figure 5c). This interaction is predominantly responsible for the most potent binding and inhibitory activity against CDK1, underscoring the significance of the 'S' atom designed in metallohelices for the precise targeting of kinase with an appropriate conformation and stereochemistry. In contrast, the thiol group of $\Delta_2\text{R}_4\text{-H}_{\text{bpy}}$ forms a single hydrogen bond with LYS9

of CDK1 at a distance of 4.0 Å. The benzene ring of $\Delta_2\text{R}_4\text{-H}_{\text{bpy}}$ engages in two carbon-hydrogen bonds with ASP86 of CDK1, with a hydrogen bond distance of 3.1 Å. Furthermore, the thiol group in $\Delta_2\text{S}_4\text{-H}_{\text{bpy}}$ is capable of forming two hydrogen bonds with LYS9 and GLU12 of CDK1, at distances of 3.7 and 3.3 Å, respectively (Figure 5d-f). This adaptability of metallohelices structure with CDK1 demonstrated our structure designability in protein targeting by introducing thiourea groups.

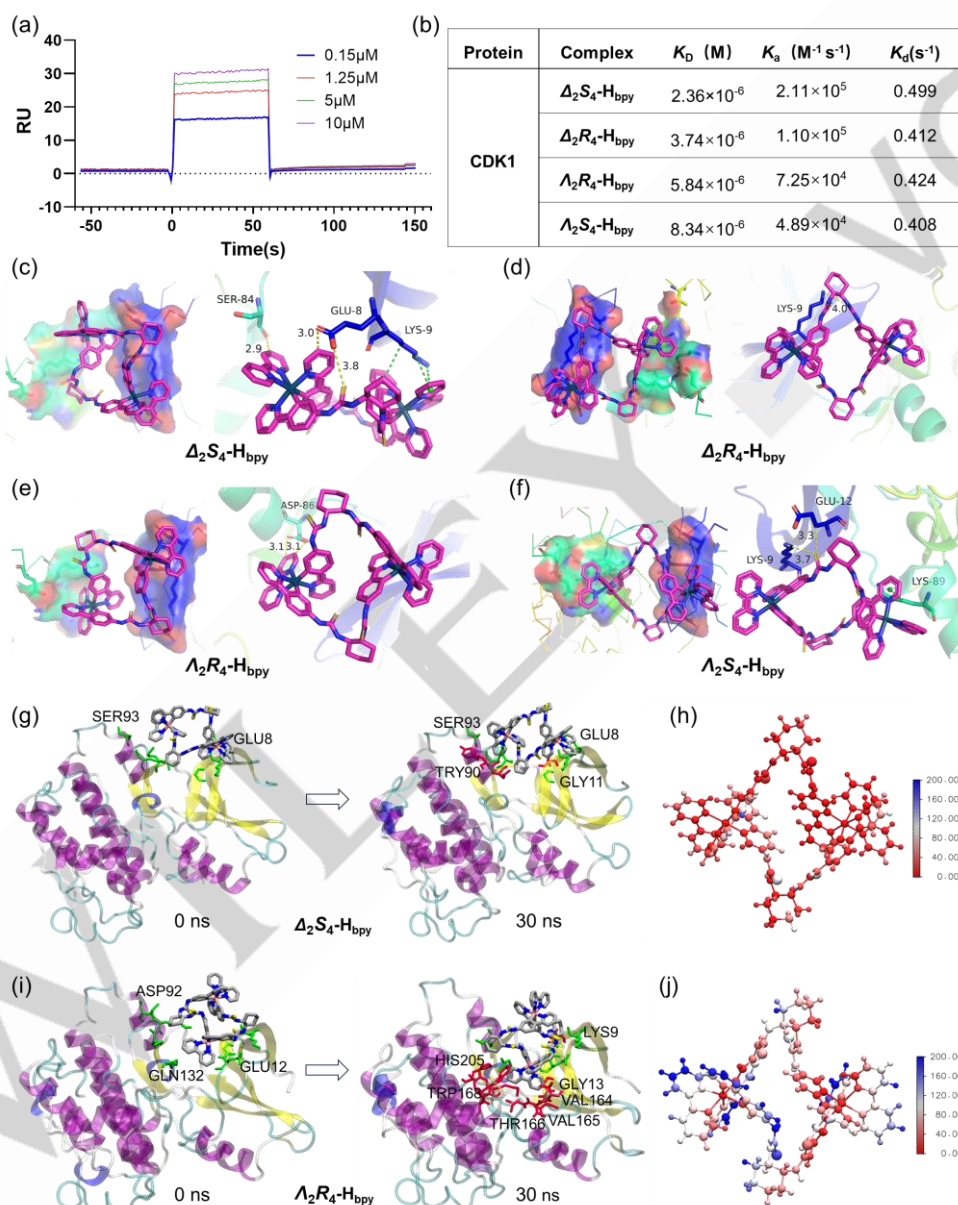


Figure 5. Binding affinity of CDK1-metallohelices by Molecular dynamic simulations and Surface Plasmon Resonance (SPR) detection. (a) Spectra of affinity assay for CDK1- $\Delta_2\text{S}_4\text{-H}_{\text{bpy}}$ interaction by SPR detection. (b) Binding affinity of metallohelices with CDK1. K_D : dissociation constant; K_A : association rate constant; K_D : dissociation rate constant. (c) Molecular docking simulations of CDK1- $\Delta_2\text{S}_4\text{-H}_{\text{bpy}}$ complexes. (d) Molecular docking simulations of CDK1- $\Delta_2\text{R}_4\text{-H}_{\text{bpy}}$ complexes. (e) Molecular docking simulations of CDK1- $\Delta_2\text{R}_4\text{-H}_{\text{bpy}}$ complexes. (f) Molecular docking simulations of CDK1- $\Delta_2\text{S}_4\text{-H}_{\text{bpy}}$ complexes. (g) Instantaneous conformations of CDK1- $\Delta_2\text{S}_4\text{-H}_{\text{bpy}}$ complex at 0 ns (the time after equilibration and before production run) and 30 ns. (h) Conformation changes of $\Delta_2\text{S}_4\text{-H}_{\text{bpy}}$ during the 30 ns molecular dynamics binding process with CDK1 (colored by the B-factor that calculated from the atomic mean square deviation value). (i) Instantaneous conformations of CDK1- $\Delta_2\text{R}_4\text{-H}_{\text{bpy}}$ complex at 0 ns (the time after equilibration and before production run) and 30 ns. (j) Conformation changes of $\Delta_2\text{R}_4\text{-H}_{\text{bpy}}$ during the 30 ns molecular dynamics binding process with CDK1 (colored by the B-factor that calculated from the atomic mean square deviation value).

RESEARCH ARTICLE

As depicted in Figure 5g-j, further molecular dynamic (MD) simulations of the binding process between $\Delta_2\text{S}_4\text{-H}_{\text{ppy}}$ / $\Lambda_2\text{R}_4\text{-H}_{\text{ppy}}$ and CDK1 during the 30 ns dynamic process were also conducted. Overlaying the final MD state structures with the docking structures visually elucidated the structural changes of metallohelicities that occurred during the interaction with CDK1, as evident in variations including Ir-Ir distances and dihedral angles formed by the two coordinated ppy ligands (Figure S118). Specifically, although $\Delta_2\text{S}_4\text{-H}_{\text{ppy}}$ presented the highest binding affinity toward CDK1, there is no obvious conformation changes during the 30 ns molecular dynamics binding process (Figure 5g-h). On the contrast, as the enantiomer of $\Delta_2\text{S}_4\text{-H}_{\text{ppy}}$, $\Lambda_2\text{R}_4\text{-H}_{\text{ppy}}$ displayed an "induce-fit" conformation adjustment to fit the target-protein 3D regions (Figure 5i-j). Notably, for both metallohelicities, van der Waals (VdW) interactions made significant contributions to the binding energy, while electrostatic interactions accounted for only a small proportion (Figure S121-122). Since VdW interactions describe weak forces between closely spaced atoms, the binding affinity between CDK1 and metallohelicities is believed to be primarily influenced by molecular shape rather than specific binding sites. These results indicated that the flexible metallohelicities may facilitate an "induce-fit" recognition process between the target protein. In this context, the metallohelicities and protein can stably bind in the case of shape adaptation. In the case of shape mismatching, the metallohelicities will adjust their conformation to fit the protein pocket, which is accompanied by the loss of stability (due to the deviation of the energy-minimized structure). All these findings underscored the capacity of $\Delta_2\text{S}_4\text{-H}_{\text{ppy}}$, attributed to its precise chiral stereochemistry, to engage in the specific interactions with CDK1, thereby inhibiting the kinase activity.

Specific Binding and Inhibition of CDK1 Reverses Metallo-drug Resistance.

As a frequently highly expressed and critically required therapeutic target in advanced cancer and malignancies,^[24] CDK1 has recently emerged as a critical mediator in the development of resistance to oxaliplatin. This resistance is attributed to the heightened expression of CDK1 in oxaliplatin-resistant cells and tissues, a phenomenon linked to the diminished presence of N6-methyladenosine modification.^[7] Consequently, the selective inhibition of CDK1 by metallohelicities, as pursued in this work, holds promise as a potential strategy to reverse the metallo-drug resistance.

We then investigated the anti-drug resistance effect of chiral metallohelicities within oxaliplatin-resistant HCT8/L cells. In contrast to the other three metallohelicities, $\Delta_2\text{S}_4\text{-H}_{\text{ppy}}$ exhibited the most potent inhibition of oxaliplatin-resistant HCT8/L cell

proliferation, with an IC₅₀ value of 18.5 nM after light irradiation, leading to a significant decrease in cell viability (Figure 6a and 6b). This effect demonstrated a pronounced chirality-dependent selectivity. Concurrently, due to the elevated expression of CDK1 in oxaliplatin-resistant HCT8/L cells, $\Delta_2\text{S}_4\text{-H}_{\text{ppy}}$, which possesses the highest affinity and targeting specificity for CDK1, was preferentially uptaken by oxaliplatin-resistant HCT8/L cells (Figure 6c). This enhanced uptake facilitated the activation of a greater quantity of reactive oxygen species (ROS), including singlet oxygen and superoxide anions during photodynamic therapy process (Figure 6d and Figure S135). Furthermore, $\Delta_2\text{S}_4\text{-H}_{\text{ppy}}$ induced a cell death morphology reminiscent of oncosis in the oxaliplatin-resistant cells. Electron microscopy revealed that cells treated with $\Delta_2\text{S}_4\text{-H}_{\text{ppy}}$ displayed numerous bubbles around the membrane region and a disappearance of mitochondria (Figure 6e-f), along with severe disruption of various intracellular organelles, which are the hallmarks of oncosis.^[25] These cumulative effects substantially contributed to the heightened inhibition of proliferation in drug-resistant cells by $\Delta_2\text{S}_4\text{-H}_{\text{ppy}}$.

Furthermore, we conducted a comprehensive validation of the inhibitory impact of $\Delta_2\text{S}_4\text{-H}_{\text{ppy}}$ on CDK1 within oxaliplatin-resistant HCT8/L cells. Preliminary evaluations employing western blot analysis confirmed that the repression of CDK1 expression by metallohelicities in these cells conformed to the expected chirality-dependent pattern, as $\Delta_2\text{S}_4\text{-H}_{\text{ppy}}$ exhibited the most pronounced inhibitory effect on CDK1 (Figure 7a and 7b). To further validate the intracellular binding of metallohelicities to CDK1, we conducted Cellular Thermal Shift Assay (CETSA) and Drug Affinity Responsive Target Stability (DARTS) experiments. These approaches are based on the premise that the stability of proteins targeted by bioactive small molecules is markedly enhanced within the cellular environment.^[26] DARTS analysis indicated that CDK1 displayed increased resistance to proteolysis in lysates derived from cells treated with $\Delta_2\text{S}_4\text{-H}_{\text{ppy}}$, as opposed to those treated with $\Delta_2\text{R}_4\text{-H}_{\text{ppy}}$, $\Lambda_2\text{R}_4\text{-H}_{\text{ppy}}$, and $\Lambda_2\text{S}_4\text{-H}_{\text{ppy}}$ (Figure 7c and 7d). A significant reduction in CDK1 expression was observed in all experimental groups with temperature increasing, suggesting a thermal destabilization effect. Notably, $\Delta_2\text{S}_4\text{-H}_{\text{ppy}}$ elicited the most substantial thermal shift for CDK1, underscoring its stronger binding affinity (Figure 7e and 7f). Collectively, these findings confirmed the specific binding of $\Delta_2\text{S}_4\text{-H}_{\text{ppy}}$ to CDK1 at the cellular level during the PDT process.

In addition, we employed intracellular proteomics to investigate the specific inhibition of $\Delta_2\text{S}_4\text{-H}_{\text{ppy}}$ to CDK1 and the subsequent intracellular pathway alterations in drug-resistant cells. Proteomic analysis revealed that CDK1 was the primary protein targeted for inhibition, with downstream pathways

RESEARCH ARTICLE

mediated by CDK1, including cell cycle progression and DNA replication, being significantly suppressed (Figure 7g-h, Figure S136-138, Table S6-S7). Gene Expression Set Analysis (GESA) further confirmed that the cell cycle process was markedly inhibited by $\Delta_2\text{S}_4\text{-H}_{\text{bpy}}$ (Figure 7i). Notably, the proteomic data indicated a substantial suppression of platinum drug resistance in

oxaliplatin-resistant HCT8/L cells, suggesting significant improvement in resistance to metallodrugs by $\Delta_2\text{S}_4\text{-H}_{\text{bpy}}$ (Figure 7h). This finding corroborates the notion that inhibition of CDK1 can significantly ameliorate metallodrug resistance and provides compelling evidence for the future development of more effective strategies to overcome metallodrug resistance.

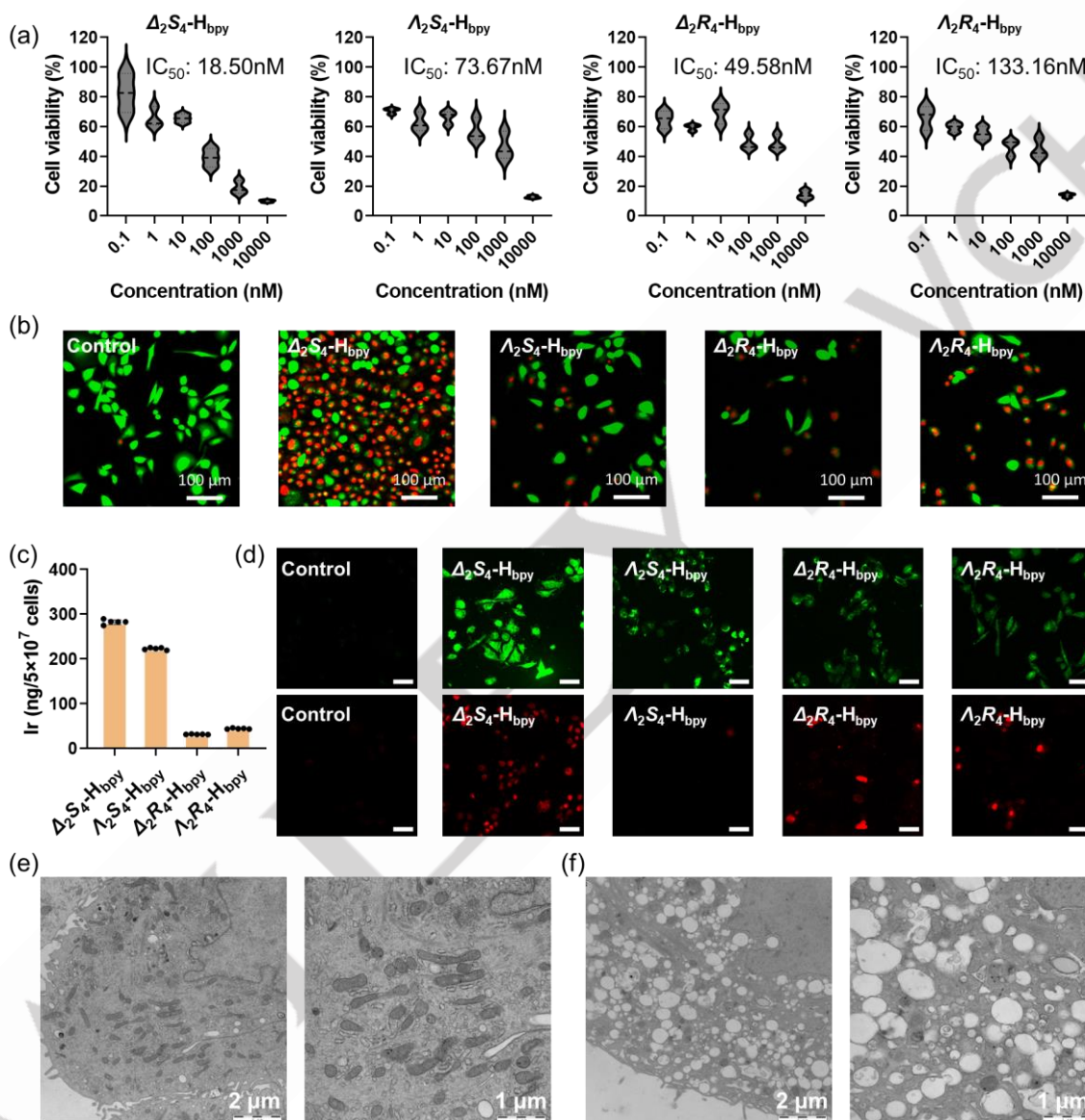


Figure 6. Chirality-dependent anticancer activity of metallohelices in CDK1-overexpressed oxaliplatin-resistant HCT8/L cells. (a) IC_{50} values and cell viability curves of $\Delta_2\text{S}_4\text{-H}_{\text{bpy}}$, $\Lambda_2\text{S}_4\text{-H}_{\text{bpy}}$, $\Delta_2\text{R}_4\text{-H}_{\text{bpy}}$ and $\Lambda_2\text{R}_4\text{-H}_{\text{bpy}}$ toward HCT8/L cells with light irradiation (white light, 30 mW/cm², 30 min). (b) Images of live and dead cells by Calcein-AM and PI staining. (c) cellular uptake of these four metallohelices by HCT8/L cells. (d) Production of singlet oxygen (up) and superoxide anions (down) in HCT8/L cells by metallohelices 12 h after irradiation (white light, 30 mW/cm², 30 min). (e) TEM images of subcellular organelle in HCT8/L cells with PBS treatment. (f) TEM images of subcellular organelle in HCT8/L cells with $\Delta_2\text{S}_4\text{-H}_{\text{bpy}}$ treatment after irradiation (white light, 30 mW/cm², 30 min).

To delineate the essential function of CDK1 in modulating the reversal of drug resistance, we performed knockdown experiments specifically directed against CDK1 within the oxaliplatin-resistant HCT8/L cells. Through the genetic suppression of CDK1, which resulted in a diminished expression

level in oxaliplatin-resistant HCT8/L cells (Figure 7j), leading to a marked reduction in the inhibitory efficacy of $\Delta_2\text{S}_4\text{-H}_{\text{bpy}}$, thereby highlighting a CDK1-dependent cytotoxic response (Figure 7k). Conversely, the remaining three other metallohelices exhibited no significant influence on the cellular viability of the drug-resistant

RESEARCH ARTICLE

cells after CDK1 silencing, pointing towards a non-CDK1-dependent mechanism of action (Figure 7I-n). Collectively, these results provide molecular and genetic validation for the notion that CDK1 inhibition is a critical determinant in the capacity of $\Delta_2S_4-H_{bpy}$ to counteract metallodrug resistance. Therefore, the

innovative design and development of the chiral metallohelices, which are designed to specifically target and inhibit the kinase activity of CDK1, present a novel perspective for the future pharmaceutical design endeavors focused on surmounting metallodrug resistance.

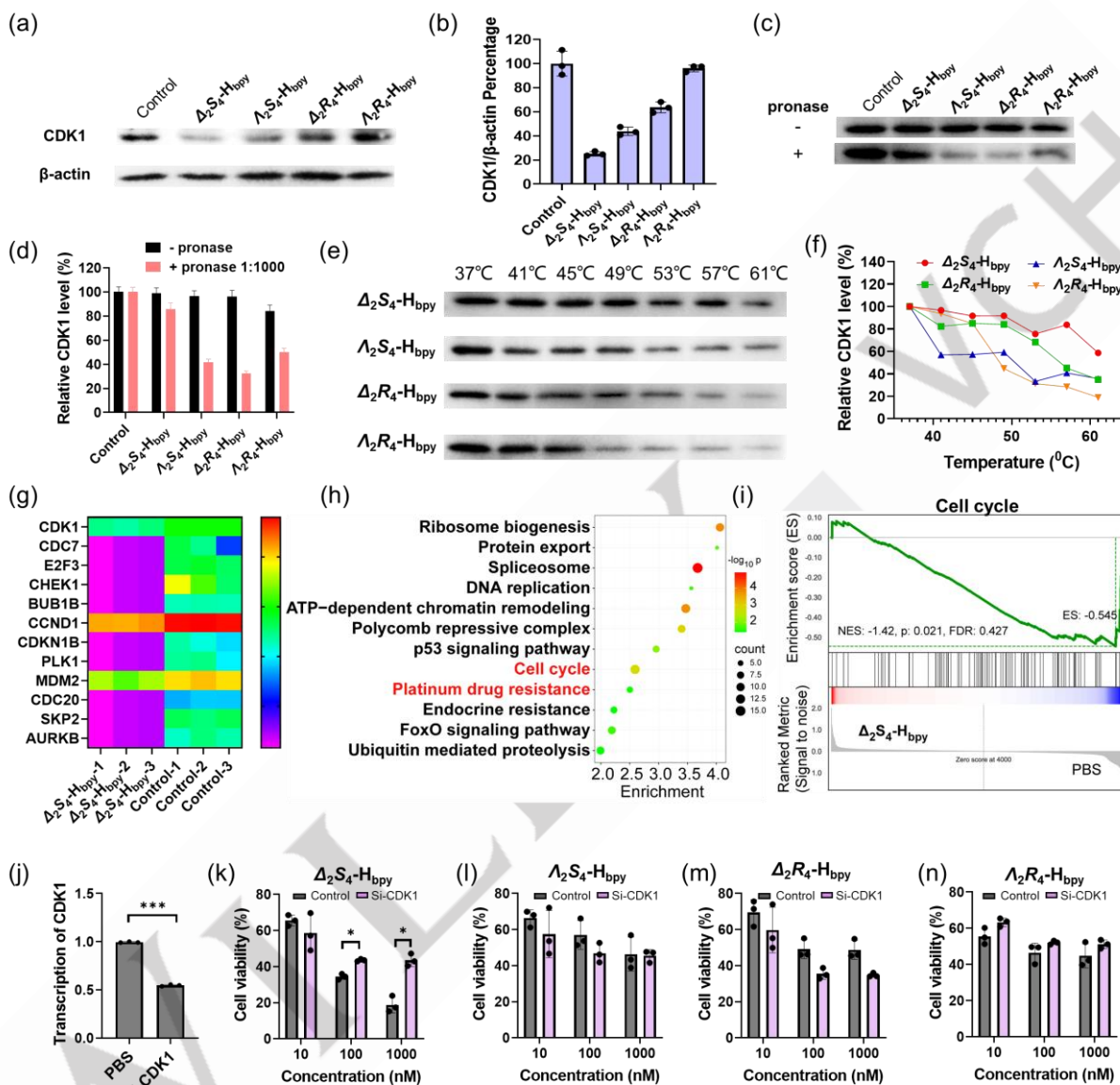


Figure 7. Chirality-dependent confirmation of CDK1 targeting of $\Delta_2S_4-H_{bpy}$ to reverse metallodrug-resistance. (a) Expression of CDK1 in PBS, $\Delta_2S_4-H_{bpy}$, $\Delta_2R_4-H_{bpy}$, $\Delta_2R_4-H_{bpy}$ and $\Delta_2S_4-H_{bpy}$ -treated oxaliplatin-resistant HCT8/L cells by western blot analysis. (b) Calculated grey-scale of each band on western blot. (c) DARTS of CDK1 in lysate of oxaliplatin-resistant HCT8/L cells treated with PBS, $\Delta_2S_4-H_{bpy}$, $\Delta_2R_4-H_{bpy}$, $\Delta_2R_4-H_{bpy}$ and $\Delta_2S_4-H_{bpy}$ followed by different concentrations of pronase E (pronase E: total protein, w/w) by western blot analysis. (d) Quantification of CDK1 expression with treatments. (e) Expression of CDK1 in lysate of HCT8/L cells treated with PBS, $\Delta_2S_4-H_{bpy}$, $\Delta_2R_4-H_{bpy}$, $\Delta_2R_4-H_{bpy}$ and $\Delta_2S_4-H_{bpy}$ at different temperature gradients by western blot analysis. (f) CETSA curves of CDK1 treated with PBS, $\Delta_2S_4-H_{bpy}$, $\Delta_2R_4-H_{bpy}$, $\Delta_2R_4-H_{bpy}$ and $\Delta_2S_4-H_{bpy}$. (g) significantly inhibited proteins in $\Delta_2S_4-H_{bpy}$ treated oxaliplatin-resistant HCT8/L cells by MS quantification. (h) KEGG pathway analysis of downregulated proteins in $\Delta_2S_4-H_{bpy}$ treated oxaliplatin-resistant HCT8/L cells. (i) GSEA analysis on the differentially expressed genes (downregulated) in cell cycle pathway in oxaliplatin-resistant HCT8/L cells treated with $\Delta_2S_4-H_{bpy}$. (j) mRNA transcription level of CDK1 in oxaliplatin-resistant HCT8/L cells after CDK1 knock down. (k) Comparison of the cell viability treated with $\Delta_2S_4-H_{bpy}$ in siCDK1 oxaliplatin-resistant HCT8/L cells and wild type (oxaliplatin-resistant HCT8/L cells). (l) Comparison of the cell viability treated with $\Delta_2S_4-H_{bpy}$ in siCDK1 oxaliplatin-resistant HCT8/L cells and wild type (oxaliplatin-resistant HCT8/L cells). (m) Comparison of the cell viability treated with $\Delta_2R_4-H_{bpy}$ in siCDK1 oxaliplatin-resistant HCT8/L cells and wild type (oxaliplatin-resistant HCT8/L cells). (n) Comparison of the cell viability treated with $\Delta_2R_4-H_{bpy}$ in siCDK1 oxaliplatin-resistant HCT8/L cells and wild type (oxaliplatin-resistant HCT8/L cells). Values are expressed as the mean \pm SD of triplicate results. Statistical significance was assessed using Student's *t*-test. * $p < 0.05$, ** $p < 0.01$, *** $p < 0.001$.

RESEARCH ARTICLE

CONCLUSIONS

In summary, we have successfully developed a novel programmable modular assembly approach for synthesizing two pairs of homochiral luminescent dinuclear Ir(III) metallohelicenes with flexible dithiourea linkages. These Ir(III) metallohelicenes demonstrated distinctive chirality-dependent anticancer efficiency *in vitro* and *in vivo*. Further investigations by proteomic screening, protein affinity analysis and molecular simulation revealed that **Δ_2S_4 -H_{bpy}**, among the resulting homochiral metallohelicenes, exhibited the highest PDT efficiency with PI value of 2.3×10^4 . This exceptional efficiency is attributed to its unique structural compatibility with accessible regions of the target CDK1 protein pockets, which underpins the distinct anticancer activities observed.

Importantly, given its role as a critical mediator in the development of oxaliplatin resistance, CDK1 targeting by **Δ_2S_4 -H_{bpy}** holds significant promise for reversing metalloidrug resistance. The high-affinity of **Δ_2S_4 -H_{bpy}** for CDK1 enhances cellular uptake and anticancer activity against oxaliplatin-resistant HCT8/L cells. Further mechanistic studies utilizing proteomic profiling and CDK1 gene silencing confirmed the essential role of chirality-selective CDK1 targeting in overcoming metalloidrug resistance. This work highlights a flexible synthetic strategy that offers a unique avenue for aligning the conformations and chirality of metallohelicenes with specific biological targets, thereby providing innovative insights into the design of metalloidrugs to reverse metalloidrug resistance.

Acknowledgements

This research work was financially supported by the National Natural Science Foundation of China (grant nos. 22477057, 22171033, 22477014, 22207053, 22025701, 22293050, 22293052, 22293053, 92353301), the National Key R&D Program of China (2023YFA1508900), the Natural Science Foundation of Jiangsu Province (BK20220764, BK20232020), Fundamental Research Funds for the Central Universities (2024300401). Special thanks to Prof. Luyang Zhao at Institute of Process Engineer-ing, Chinese Academy of Sciences for the help of DFT calculations. We thank Prof. Rong Zhang at the State Key Laboratory of Fine Chemicals, Dalian University of Technology for the help with HR-ESI-MS analysis, and Dr. Cai Rui in Instrumental Analysis Center of Dalian University of Technology for the assistance with photoluminescence spectra analysis.

Conflict of Interest

The authors declare no conflict of interest.

Data Availability Statement

The data that support the findings of this study are available in the supporting material of this article.

Keywords: Metalloidrug Resistance • Chirality • Ir(III) metallohelicenes • CDK1-Targeting • Photodynamic Therapy

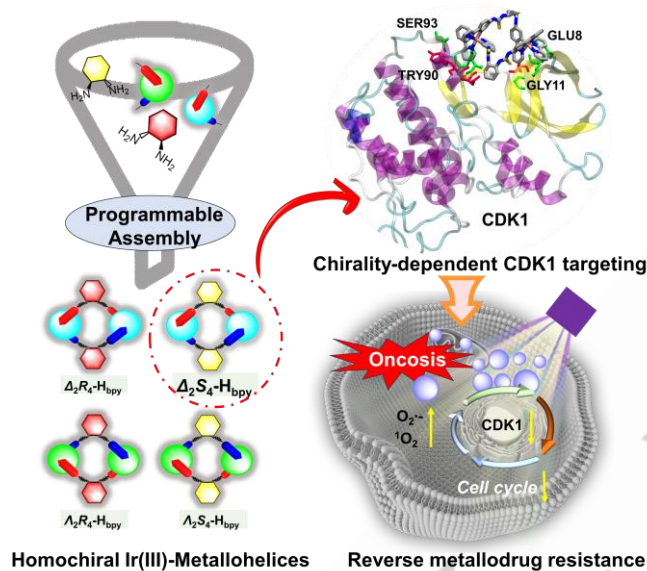
- [1] T. C. Johnstone, G. Y. Park, S. J. Lippard, *Anticancer Res.* **2014**, *34*, 471-476.
- [2] a) D. Wang, S. J. Lippard, *Nat. Rev. Drug Discov.* **2005**, *4*, 307-320; b) B. J. Pages, D. L. Ang, E. P. Wright, J. R. Aldrich-Wright, *Dalton Trans.* **2015**, *44*, 3505-3526.
- [3] X. Z. Li, X. Zhao, W. Wang, Z. L. Shi, Y. M. Zhang, Q. Q. Tian, Y. G. Yao, C. He, C. Y. Duan, *Coord. Chem. Rev.* **2023**, *495*, 215366.
- [4] a) D. E. Dolmans, D. Fukumura, R. K. Jain, *Nat. Rev. Cancer.* **2003**, *3*, 380-387; b) A. P. Castano, P. Mroz, M. R. Hamblin, *Nat. Rev. Cancer.* **2006**, *6*, 535-545.
- [5] B. Q. Spring, I. Rizvi, N. Xu, T. Hasan, *Photochem. Photobiol. Sci.* **2015**, *14*, 1476-1491.
- [6] B. Tang, D. Wan, Y. J. Wang, Q. Y. Yi, B. H. Guo, Y. J. Liu, *Eur. J. Med. Chem.* **2018**, *145*, 302-314.
- [7] K. Zeng, W. Li, Y. Wang, Z. Zhang, L. Zhang, W. Zhang, Y. Xing, C. Zhou, *Adv. Sci.* **2023**, *10*, e2301088.
- [8] a) L. Feng, Y. Geisselbrecht, S. Blanck, A. Wilbuer, G. E. Atilla-Gokcumen, P. Filippakopoulos, K. Kräling, M. A. Celik, K. Harms, J. Maksimoska, R. Marmorstein, G. Frenking, S. Knapp, L. O. Essen, E. Meggers, *J. Am. Chem. Soc.* **2011**, *133*, 5976-5986; b) A. Wilbuer, D. H. Vlecken, D. J. Schmitz, K. Kräling, K. Harms, C. P. Bagowski, E. Meggers, *Angew. Chem., Int. Ed.* **2010**, *49*, 3839-3842; c) C. H. Leung, H. J. Zhong, H. Yang, Z. Cheng, D. S. H. Chan, V. P. Y. Ma, R. Abagyan, C. Y. Wong, D. L. Ma, *Angew. Chem., Int. Ed.* **2012**, *51*, 9010-9014; d) G. D. Li, C. N. Ko, D. Li, C. Yang, W. H. Wang, G. J. Yang, C. Di Primo, V. K. W. Wong, Y. Z. Xiang, L. G. Lin, D. L. Ma, C. H. Leung, *Nat. Commun.* **2021**, *12*, 3363.
- [9] R. Rajaratnam, E. K. Martin, M. Dörr, K. Harms, A. Casini, E. Meggers, *Inorg. Chem.* **2015**, *54*, 8111-8120.
- [10] Y. J. Wang, M. M. Dix, G. Bianco, J. R. Remsberg, H. Y. Lee, M. Kalocsay, S. P. Gygi, S. Forli, G. Vite, R. M. Lawrence, C. G. Parker, B. F. Cravatt, *Nat. Chem.* **2019**, *11*, 1113-1123.
- [11] a) T. R. Cook, P. J. Stang, *Chem. Rev.* **2015**, *115*, 7001-7045; b) R. Kieleyka, P. Englebienne, J. Fakhoury, C. Autexier, N. Moitessier, H. F. Sleiman, *J. Am. Chem. Soc.* **2008**, *130*, 10040-10041; c) M. Li, S. E. Howson, K. Dong, N. Gao, J. S. Ren, P. Scott, X. G. Qu, *J. Am. Chem. Soc.* **2014**, *136*, 11655-11663; d) K. Wu, K. Li, Y. J. Hou, M. Pan, L. Y. Zhang, L. Chen, C. Y. Su, *Nat. Commun.* **2016**, *7*, 10487; e) Y. L. Lu, Y. P. Wang, K. Wu, M. Pan, C. Y. Su, *Acc. Chem. Res.*, **2024**, *57*, 3277-3291.
- [12] a) J. M. Lehn, A. Rigault, J. Siegel, J. Harrowfield, B. Chevrier, D. Moras, *P Natl. Acad. Sci. USA.* **1987**, *84*, 2565-2569; b) M. J. Hannon, L. J. Childs, *Supramol. Chem.* **2004**, *16*, 7-22; c) M. Albrecht, *Chem. Rev.* **2001**, *101*, 3457-3497; d) H. Song, M. Postings, P. Scott, N. J. Rogers, *Chem. Sci.* **2021**, *12*, 1620-1631.
- [13] a) E. M. Driggers, S. P. Hale, J. Lee, N. K. Terrett, *Nat. Rev. Drug Discov.* **2008**, *7*, 608-624; b) E. A. Villar, D. Beglov, S. Chennamadhavuni, J. A. Porco, D. Kozakov, S. Vajda, A. Whitty, *Nat. Chem. Biol.* **2014**, *10*, 723-731; c) L. Tan, M. Sun, H. Wang, J. Wang, J. Kim, M. Lee, *Nat. Synth.* **2023**, *2*, 1222-1231.
- [14] a) M. J. Hannon, V. Moreno, M. J. Prieto, E. Moldrheim, E. Sletten, I. Meistermann, C. J. Isaac, K. J. Sanders, A. Rodger, *Angew. Chem. Int. Ed.* **2001**, *40*, 880-884; b) S. E. Howson, A. Bolhuis, V. Brabec, G. J. Clarkson, J. Malina, A. Rodger, P. Scott, *Nat. Chem.* **2011**, *4*, 31-36; c) A. D. Faulkner, R. A. Kaner, Q. M. A. Abdallah, G. Clarkson, D. J. Fox, P. Gurnani, S. E. Howson, R. M. Phillips, D. I. Roper, D. H. Simpson, P. Scott, *Nat. Chem.* **2014**, *6*, 797-803; d) C. Q. Zhao, H. L. Song, P. Scott, A. D. Zhao, H. Tateishi-Karimata, N. Sugimoto, J. S. Ren, X. G. Qu, *Angew. Chem. Int. Ed.* **2018**, *57*, 15723-15727; e) X. Z. Li, J. G. Wu, L. Wang, C. He, L. Y. Chen, Y. Jiao, C. Y. Duan, *Angew. Chem. Int. Ed.* **2020**, *59*, 6420-6427; f) X. Li, Z. Wang, X. Hao, J. Zhang, X. Zhao, Y. Yao, W. Wei, R. Cai, C. He, C.

RESEARCH ARTICLE

- Duan, Z. Guo, J. Zhao, X. Wang, *J. Am. Chem. Soc.* **2023**, *145*, 14766-14775.
- [15] R. A. Kaner, P. Scott, *Future Med Chem.* **2015**, *7*, 1-4.
- [16] a) D. D. Boehr, R. Nussinov, P. E. Wright, *Nat. Chem. Biol.* **2009**, *5*, 954-954; b) A. Stank, D. B. Kokh, J. C. Fuller, R. C. Wade, *Acc. Chem. Res.* **2016**, *49*, 809-815; c) S. Chen, D. Bertoldo, A. Angelini, F. Pojer, C. Heinis, *Angew. Chem. Int. Ed.* **2014**, *53*, 1602-1606.
- [17] a) J. R. Aldrich-Wright, *Nat. Chem.* **2012**, *4*, 10-11; b) S. E. Howson, P. Scott, *Dalton Trans.* **2011**, *40*, 10268-10277.
- [18] a) D. P. Zhao, T. van Leeuwen, J. L. Cheng, B. L. Feringa, *Nat. Chem.* **2017**, *9*, 250-256; b) H. Miyake, H. Tsukube, *Chem. Soc. Rev.* **2012**, *41*, 6977-6991; c) Z. Y. Lv, Z. H. Chen, K. N. Shao, G. Y. Qing, T. L. Sun, *Polymers-Basel* **2016**, *8*, 310.
- [19] a) C. He, Y. G. Zhao, D. Guo, Z. H. Lin, C. Y. Duan, *Eur. J. Inorg. Chem.* **2007**, 3451-3463; b) A. Lützen, M. Hapke, J. Griep-Raming, D. Haase, W. Saak, *Angew. Chem., Int. Ed.* **2002**, *41*, 2086-2089.
- [20] J. G. Wu, X. Z. Li, P. Y. Wu, Z. L. Shi, L. Y. Chen, R. Zhang, C. He, C. Y. Duan, *Chem. Mater.* **2022**, *34*, 4471-4478.
- [21] M. Helms, C. Y. Wang, B. Orth, K. Harms, E. Meggers, *Eur. J. Inorg. Chem.* **2016**, 2896-2901.
- [22] X. Z. Li, Z. L. Shi, J. G. Wu, J. L. Wu, C. He, X. R. Hao, C. Y. Duan, *Chem. Commun.* **2020**, *56*, 7537-7548.
- [23] a) L. B. Ke, F. M. Wei, L. N. Xie, J. Karges, Y. Chen, L. N. Ji, H. Chao, *Angew. Chem. Int. Ed.* **2022**, *61*, e202205429; b) S. Kuang, F. M. Wei, J. Karges, L. B. Ke, K. Xiong, X. X. Liao, G. Gasser, L. N. Ji, H. Chao, *J. Am. Chem. Soc.* **2022**, *144*, 4091-4101.
- [24] a) X. J. Lu, Y. Z. Pang, H. Cao, X. X. Liu, L. Tu, Y. Y. Shen, X. N. Jia, J. C. Lee, Y. X. Wang, *Cancer Research* **2021**, *81*, 2481-2494; b) U. Asghar, A. K. Witkiewicz, N. C. Turner, E. S. Knudsen, *Nat. Rev. Drug. Discov.* **2015**, *14*, 130-146.
- [25] T. Feng, Z. X. Tang, J. Shu, X. B. Wu, H. Jiang, Z. L. Chen, Y. Chen, L. N. Ji, H. Chao, *Angew. Chem. Int. Ed.* **2024**, *63*, e202405679.
- [26] a) Y. S. Ren, H. L. Li, X. H. Piao, Z. Y. Yang, S. M. Wang, Y. W. Ge, *Biochem Pharmacol.* **2021**, *194*; b) S. Mozaffari-Jovin, T. Wandersleben, K. F. Santos, C. L. Will, R. Lührmann, M. C. Wahl, *Science* **2013**, *341*, 80-84.

RESEARCH ARTICLE

Entry for the Table of Contents



A novel programmable modular assembly method was developed for the construction of homochiral, luminescent dinuclear Ir(III) metallohelices with flexible dithioureia linkages. The metallohelices exhibit significant chirality-dependent photocytotoxicities and CDK1-specific targeting ability, offering innovative insights into the design of chiral helical metallodrugs aimed at reversing metal drug resistance.